nature communications

Article

https://doi.org/10.1038/s41467-025-68067-8

Unconventional hysteresis due to time-reversal symmetry breaking superconductivity in RbV_3Sb_5

Received: 4 November 2024

Accepted: 16 December 2025

Shuo Wang[1,7], Xilin Feng[2,7], Jing-Zhi Fang[1,7], Jia-Peng Peng[3], Zi-Ting Sun[2], Jia-Jie Yang[3], Liang Xiong[3], Jingchao Liu[4], Jia-Ji Zhao[5], Ning Kang[6], Xiao-Song Wu[5], Zhensheng Zhang[1], Xuewen Fu[4], Kam Tuen Law[2] ✉, Ben-Chuan Lin[1] ✉ & Dapeng Yu[1] ✉

The study of kagome materials has recently attracted much attention due to the presence of many electron-electron interaction-driven phases in a single material. In this work, we report the time-reversal symmetry-breaking superconductivity in the thin-flake kagome material RbV_3Sb_5. Firstly, when an in-plane magnetic field is swept in opposite directions, we observe an unconventional form of hysteresis in magnetoresistance, which is different from the hysteresis induced by extrinsic mechanisms. In contrast, no such hysteresis is observed in CsV_3Sb_5 samples below their superconducting transition temperature. Strikingly, at a fixed magnetic field, the finite-resistance state in RbV_3Sb_5 can be transitioned into the superconducting state by applying and subsequently removing a large current. Secondly, at temperatures around 400 mK, the re-entrance of superconductivity occurs during an in-plane field-sweeping process with a fixed sweeping direction. The observations of the unconventional hysteresis and re-entrance suggest the existence of time-reversal symmetry-breaking superconducting states in RbV_3Sb_5.

The discovery of kagome superconductors[1–4] AV_3Sb_5 (A = K, Rb, Cs) has garnered significant attention in recent years due to their intriguing interplay of superconductivity[5–14], charge density waves[5,15–25], nematic orders[20,23], pair density waves[6,12,13], all within a single material. Such intricate interplay of the intertwined orders holds promise for uncovering unconventional phenomena, notably unconventional superconductivity[5–14]. Indeed, the nodal superconducting states have been observed in the kagome superconductor RbV_3Sb_5 with μSR experiments[9], while nodeless superconductivity was suggested in the CsV_3Sb_5 compound[26–29]. Up to now, the mechanism of the superconducting properties of the AV_3Sb_5 family remains an open question[4], necessitating further investigation and exploration.

Here, we report the unconventional superconductivity in the kagome material RbV_3Sb_5. The observed superconducting states in RbV_3Sb_5 are characterized by the emergence of the in-plane magnetic field-driven unconventional hysteresis in the resistance measurements, followed by the zero-field superconducting diode effect observed in an irradiated RbV_3Sb_5 sample that breaks inversion symmetry. In addition, by heating the sample with a large current and subsequently removing it, all at a fixed magnetic field within the hysteresis loop, the sample can be brought from a finite-resistance state to

---

[1]International Quantum Academy, and Shenzhen Branch, Hefei National Laboratory, Shenzhen, China. [2]Department of Physics, Hong Kong University of Science and Technology, Clear Water Bay, Hong Kong, China. [3]Southern University of Science and Technology, Shenzhen, China. [4]Ultrafast Electron Microscopy Laboratory, The MOE Key Laboratory of Weak-Light Nonlinear Photonics, School of Physics, Nankai University, Tianjin, China. [5]State Key Laboratory for Artificial Microstructure and Mesoscopic Physics, Frontiers Science Center for Nano-optoelectronics, Peking University, Beijing, China. [6]Key Laboratory for the Physics and Chemistry of Nanodevices, School of Electronics, Peking University, Beijing, China. [7]These authors contributed equally: Shuo Wang, Xilin Feng, Jing-Zhi Fang. ✉e-mail: phlaw@ust.hk; linbenchuan@iqasz.cn; yudapeng@iqasz.cn

a superconducting state. Moreover, an asymmetric re-entrance of superconductivity driven by the in-plane magnetic field is observed at around 400 mK, showing two superconducting domes in the temperature-magnetic field phase diagram. Through magnetotransport experiments, we observe a distinct anisotropic two-fold symmetry of the in-plane upper critical fields in this centrosymmetric material. These findings underscore the unconventional and time-reversal symmetry breaking nature of superconductivity in RbV_3Sb_5.

Basic superconducting properties

The kagome family AV_3Sb_5 represents a class of layered kagome superconductors, characterized by the alternating arrangement of V-Sb slabs, Sb slabs and A slabs. Specifically, RbV_3Sb_5 is a member of this family, which consists of V-Sb slabs interleaved with Rb layers. Each V-Sb slab exhibits a two-dimensional (2D) kagome net of V atoms, with Sb atoms occupying central positions of hexagons within the kagome lattice, as depicted in Fig. 1a. Evidently, this structural arrangement signifies a six-fold rotational symmetry. Figure 1b shows the calculated energy band of the kagome superconductor, highlighting an important feature near the Fermi energy: the parity mixing between the d-orbital of the V atom and the p-orbital of the Sb atom, introducing a spin-orbit-parity-coupling term[30,31] in contrast to the conventional spin-orbit-coupling term. In the two-dimensional limit, this spin-orbit-parity-coupling term is responsible for the observation of the two-fold symmetric in-plane upper critical field in this centrosymmetric material[30,31] which exhibits a nematic normal state[20]. In Fig. 1c, we present the current-voltage curves of the device at different temperatures, showcasing a characteristic superconducting behavior. Correspondingly, Fig. S1 shows the device image, in which the x-axis is roughly along the source-drain direction and the long axis of the sample. Figure 1d depicts the typical in-plane magnetic field dependence of the differential resistance dV/dI at a temperature T = 150 mK. Apparently, the critical current decreases with the magnetic field increasing, a hallmark of superconducting behavior. The in-plane superconducting coherence length is estimated to be around 137 nm according to the linearized Ginzburg–Landau (GL) expression[32] $B_{C\perp}=\Phi_0/2\pi\xi_0^2\,(1-T/T_C)$, where Φ_0 is the magnetic flux quantum, ξ_0 is the zero-temperature in-plane coherence length, and T_c is the critical temperature, as shown in Fig. S2.

Unconventional hysteretic superconducting behavior

We proceed by investigating the magnetic field dependence of the kagome superconductor RbV_3Sb_5. The configuration of the device is depicted in Fig. 2a. We employ a three-dimensional (3D) vector magnetic field to study the magnetic response of the superconducting states. In Fig. 2a, the direction of the magnetic field is defined by the θ

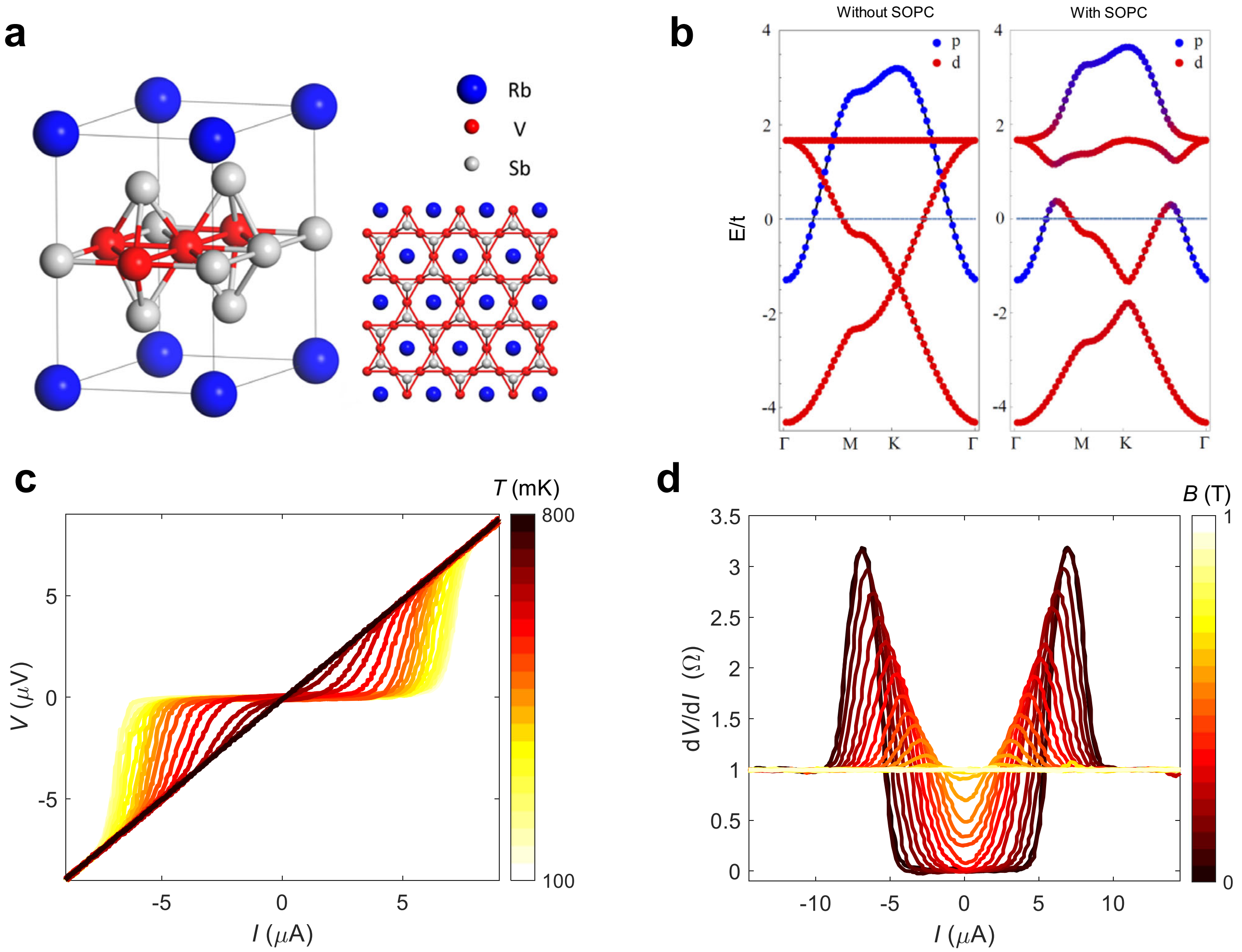

Fig. 1 | The crystal structure and superconducting behavior of RbV_3Sb_5. **a** The crystal structure of the kagome material RbV_3Sb_5. **b** The band structure of the minimal four-band model describing the in-plane properties of the kagome superconductor without (left) and with (right) spin-orbital-parity coupling (SOPC) effect, respectively. The SOPC leads to the mixing of the d-orbital belonging to V atoms and the p-orbital belonging to Sb atoms near the Fermi energy. Here, t represents the hopping strength between the nearest-neighbor V atoms. **c** The current-voltage curve at different temperatures. **d** The differential resistance dV/dI versus bias current I as a function of the magnetic field at 150 mK shows the typical superconducting behavior.

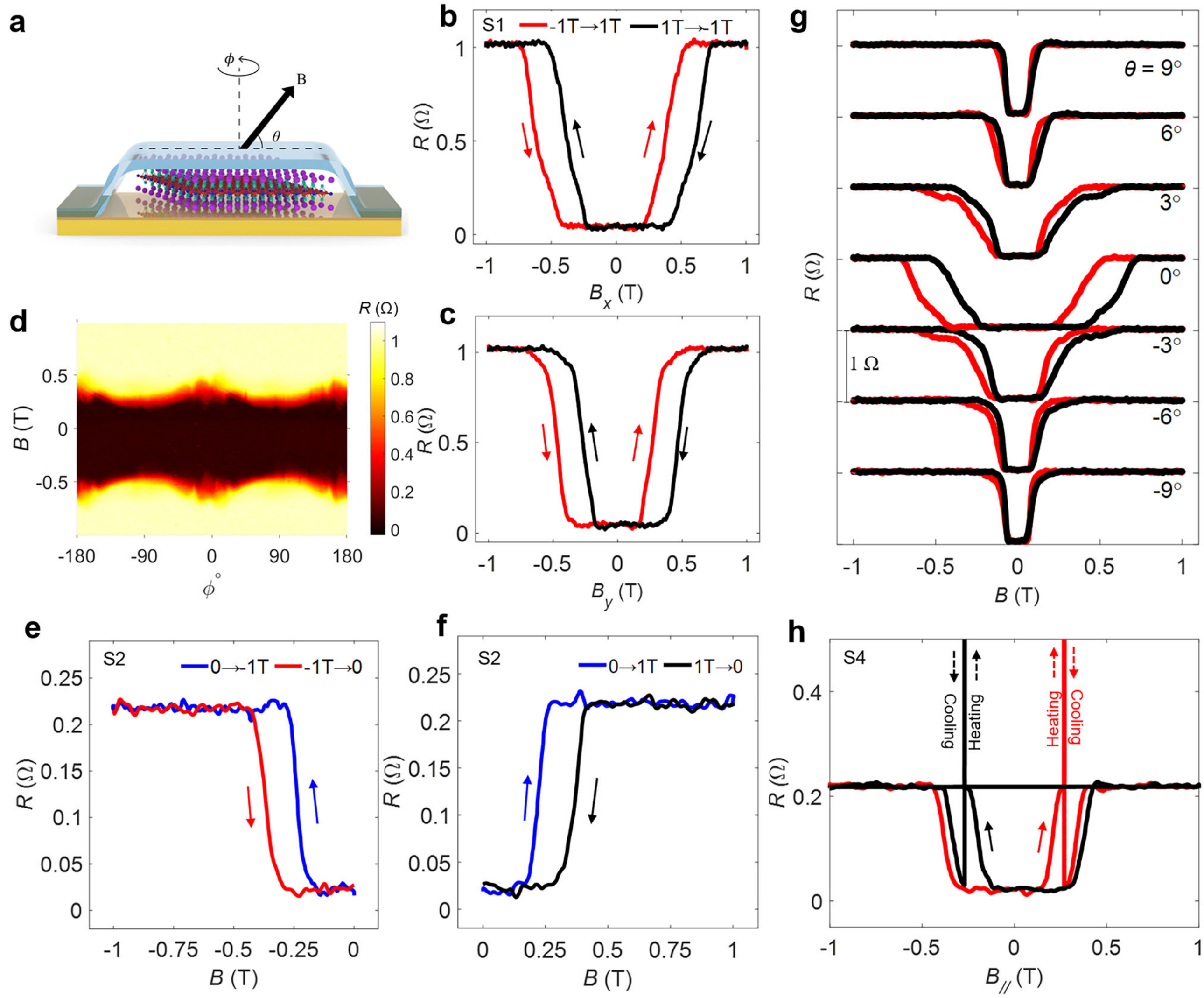

Fig. 2 | The hysteretic behavior of the superconducting states. a The schematics of the device. **b**, **c**, The in-plane magnetic field dependence of the magnetoresistance shows the hysteretic behavior along x-axis and y-axis. The temperature is 150 mK. Notably, the critical field values—defined by the magnitude of the magnetic field at which the resistance reaches 50% of the normal state resistance at the positive magnetic field—during forward (denoted as $B_{\rightarrow}$) and backward ($B_{\leftarrow}$) sweeps exhibit $B_{\rightarrow} < B_{\leftarrow}$. **d**, The mapping plot of the magnetoresistance versus the magnetic field and its direction. **e**, **f** The magnetoresistance curve measured during the field-sweeping process of sample S2: the two blue curves, positioned on either side of the B = 0 axis, representing the cases where the field is swept from 0 T to 1 T and from 0 T to −1 T, respectively. The red and black curves represent the magnetoresistance measured when the field is swept from −1 T to 0 T and 1 T to 0 T, respectively. **g**, The out-of-plane angle dependence of the magnetoresistance. **h**, The current heating and cooling process of the hysteresis in resistance as a function of the in-plane magnetic field at a temperature of 230 mK. A large current is applied at a finite resistance state to heat up the sample. After the current is removed, the sample transits to a superconducting state.

and ϕ which are the polar angle and the azimuthal angle, respectively. Specifically, $\theta = \phi = 0^\circ$ denotes the direction of the x-axis. Remarkably, the magnetoresistance curve exhibits pronounced hysteretic behavior, as illustrated in Fig. 2b. When an in-plane magnetic field oriented along the x-direction is swept from −1 T to 1 T (red curve), the superconducting state is initially established at around −410 mT; then as the magnetic field turns positive, the resistance deviates from zero at about 210 mT, exhibiting pronounced asymmetry. Moreover, sweeping the field from 1 T back to −1 T (black curve), produces a mirrored response, thus uncovering hysteretic behavior. If we define the critical magnetic field by the magnitude of the magnetic field at which the resistance reaches 50% of the normal state resistance, then we get the critical values at the positive magnetic field during forward (denoted as $B_{\rightarrow}$) and backward ($B_{\leftarrow}$) sweeps as $B_{\rightarrow} = 380$ mT and $B_{\leftarrow} = 620$ mT, respectively. Similar hysteresis is also observed when the magnetic field is applied along the y-axis as depicted in Fig. 2c. Figure 2e, f further show the hysteretic behavior observed during the field sweeping from 0 T to −1 T or 1 T, respectively. Notably, the critical field in the forward sweep is smaller than that in the backward sweep ($B_{\rightarrow} < B_{\leftarrow}$), in sharp contrast to the trivial magnetic hysteresis ($B_{\rightarrow} > B_{\leftarrow}$) typically observed in conventional superconductors[33,34]. This unusual behavior, as will be discussed later, points to broken time-reversal symmetry in the superconducting state. Additional evidence for such symmetry breaking is provided by the zero-field superconducting diode effect observed in the irradiated RbV_3Sb_5 sample that breaks inversion symmetry (Fig. S3).

A natural question is whether such hysteretic behavior is exclusively confined to the in-plane orientation. To answer this question, we conduct the out-of-plane magnetic field angle dependence of the hysteresis. As depicted in Fig. 2g, our findings demonstrate that at an out-of-plane angle θ = ±9 °, the hysteresis is destroyed. Such out-of-plane magnetic field angle dependence suggests that the hysteresis is related to the in-plane magnetization of the superconducting state. Consequently, this rules out the possibility that the hysteresis is triggered by the out-of-plane component of the magnetic field.

The two-fold symmetric upper critical field

We further study the ϕ-dependence of the magnetoresistance under the in-plane magnetic field. The magnetoresistance as a function of ϕ are shown in Fig. 2d. A distinct two-fold symmetric behavior is evident. The extraction of the upper critical fields is further illustrated in Fig. S4a. As shown in the theoretical calculations (Fig. S4b) within the single-layer limit, the presence of the nematic order and the spin-orbit-parity-coupling (SOPC)[30,31] can lead to a two-fold symmetric upper critical field (details can be found in the Supplementary Information) even when the orbital effects of the in-plane magnetic field are ignored. Due to the finite thickness of the sample, the orbital effects of the magnetic field can also induce this two-fold symmetry[35,36], given the six-fold rotational symmetry is broken by the nematic order in the normal state[20]. The extra contribution of the orbital effect only changes the results quantitatively. The key conclusion of observed two-fold symmetric upper critical field is that the original D_{6h} point group symmetry is reduced to D_{2h} due to the presence of the nematic state.

The current heating and cooling experiment

In Fig. 2h, the result of the current heating and cooling experiment is depicted. Initially, as the magnetic field sweeps from −1 T to 270 mT (illustrated by the red curve) and the system enters into the state with non-zero resistance. At this point, we apply a large current to heat up the sample to suppress superconductivity completely. Subsequently, removing the current allows the system to cool down and enter into the superconducting state, as indicated by the red curve. Notably, with further increasing the magnetic field to 1 T, the resistance curve closely resembles the one observed during the magnetic field's reversal from 1 T to 270 mT (shown by black curve). Furthermore, by repeating the current heating and cooling experiment while sweeping the magnetic field from 1 T to −270 mT (black curve), a similar phenomenon is observed. This finding clearly shows that the finite-resistance state within the hysteresis loop is a metastable state which has a higher energy than the ground state. As will be discussed below, this observation provides crucial evidence for the existence of superconducting domains in the sample.

Magnetic field driven re-entrance of superconductivity

Subsequently, an investigation into the temperature dependence of the magnetoresistance is studied. As temperature rises, superconductivity can be suppressed by thermal effects. Figure 3a, b show the temperature-magnetic field phase diagram and waterfall plot of the temperature dependence of the magnetoresistance curve, respectively, while the complete temperature-magnetic field phase diagram is available in the supplementary Fig. S6a. Remarkably, within Fig.3a, two distinct superconducting domes are observed in the magnetoresistance measurements when the magnetic field changes from −1 T to 1 T. Initially, the superconductivity is destroyed at a finite magnetic field of 80 mT at 400 mK. However, a second dome of superconductivity is observed when the magnetic field becomes larger in the positive direction. Such a phenomenon of re-entrant superconductivity persists across a temperature span from 400 mK to 600 mK. When the sweep direction of the magnetic field is reversed, the corresponding mapping figure will be mirrored, as shown in Fig. S6b. Furthermore, the re-entrant superconducting states are also observed for magnetic fields in all in-plane directions, corroborated in the supplementary Fig. S7. We label these two distinct superconducting phases as "SC-I" (the superconducting dome obtained

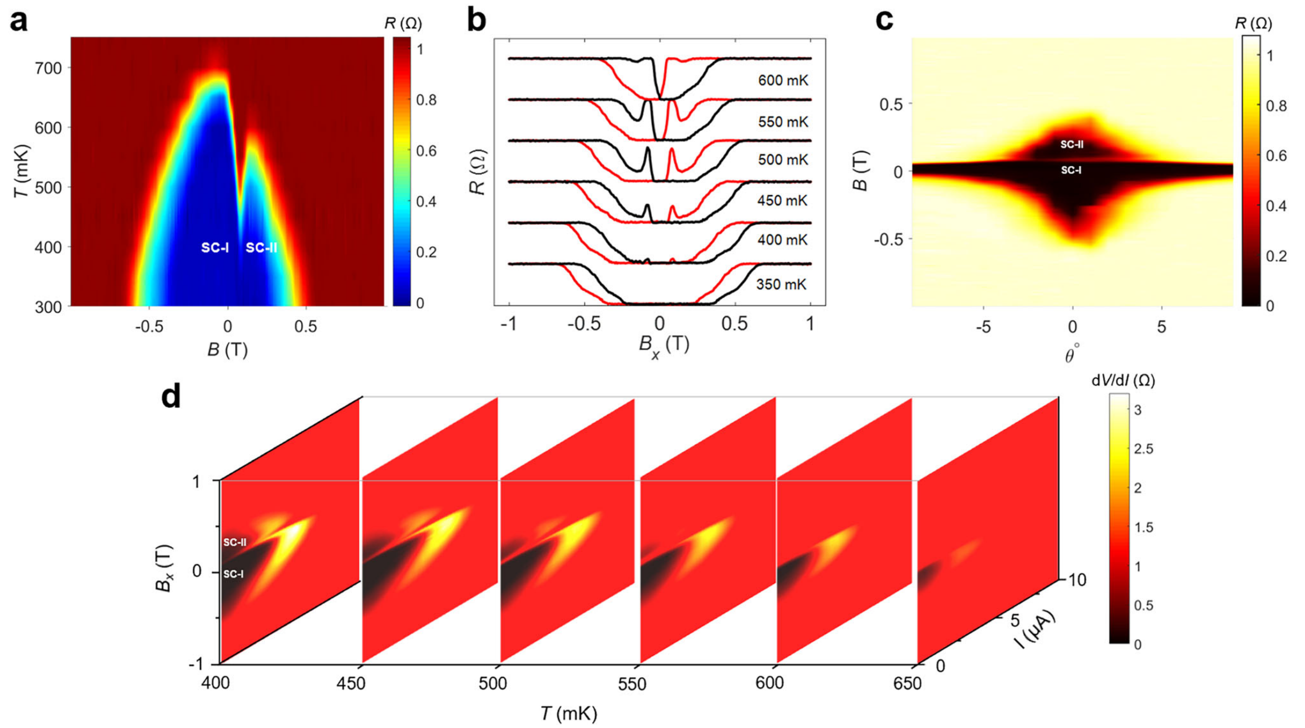

Fig. 3 | The re-entrant superconductivity. a The temperature dependence of the magnetoresistance when the magnetic field sweeps from −1 T to 1 T. With temperature increasing, the critical magnetic field gradually decreases. However, a re-entrant superconductivitssy occurs at around 400 mK. Here we label the superconducting dome obtained before the re-entrance of superconductivity as SC-I and the superconducting dome obtained after the re-entrance of superconductivity as SC-II. **b** The waterfall plot of the resistance at different temperatures. It is evident that the re-entrant superconductivity starts at 400 mK. The red curves denote a forward sweep, while the black curves represent a backward sweep. **c** The out-of-plane angle dependence of two superconducting states at a temperature of 400 mK. **d** The temperature dependence of the mapping plot of the two superconducting states versus the magnetic field and bias current.

before the re-entrance of superconductivity) and “SC-II” (the superconducting dome obtained after the re-entrance of superconductivity) as shown in Fig. 3a. The temperature dependence of the re-entrant behavior is shown in Fig. 3b.

Figure 3c shows the θ-dependence of the magnetoresistance. It is shown that superconductivity in SC-II is eliminated when the out-of-plane magnetic field angle exceeds 6° while SC-I still exists. This observation underscores the greater fragility of SC-II to out-of-plane magnetic field components. To further display the two superconducting domes SC-I and SC-II of the material, we measure dV/dI as a function of the magnetic field and applied current at different temperatures[37] as shown in Fig. 3d. Two superconducting domes SC-I and SC-II are clearly observed. Similar hysteresis and re-entrant behavior are reproduced and Figs. S8, 9 show the results for samples #2 and #3.

Ruling out trivial origins

Although hysteresis in magnetoresistance can be induced by superheating and supercooling effects[33,34] or the flux-trapping effects[38–40] as shown in previous works, the hysteresis loops observed in Fig. 2 are distinct from the hysteresis observed in previous experiments.

In the hysteresis induced by the superheating-supercooling effect, sweeping the magnetic field from 0 T to 1 T (forward sweep) and then gradually reducing the magnetic field from 1 T back to 0 T (backward sweep) must result in a higher upper critical field during the forward sweep compared to the backward sweep[33]. In contrast, our observations, as illustrated in Fig. 2f, reveal that during the forward sweep from 0 T to 1 T (indicated by the blue curve), the upper critical field B_0 is smaller than the upper critical field $B_{\leftarrow}$ in the backward sweep (indicated by the black curve). The same result is obtained when the magnetic field is swept from 0 T to −1 T and then reduced gradually, as shown in Fig. 2e by the blue and red curves. Such findings exclude the superheating and supercooling mechanism caused by the magnetic field induced local minima of the free energy of the superconductor[41].

In addition, the hysteresis observed in our experiment exhibits behavior starkly distinct from that attributed to the flux-trapping mechanism. In the hysteresis induced by the flux-trapping, a magnetoresistance minimum at finite magnetic field can be observed in the backward-sweeping curve (returning curve)[40,42,43]. In contrast, as shown in Fig. 2b, c and Fig. S10 in Supplementary Information, in RbV_3Sb_5, no magnetoresistance minimum at finite field was observed in the backward-sweeping curve over a wide range of applied currents.

Moreover, we conducted in-plane field-sweep experiments on over ten thin-flake kagome material CsV_3Sb_5. Although RbV_3Sb_5 and CsV_3Sb_5 belong to the same kagome material family and the thin flakes we used have similar thicknesses, no such hysteresis was observed in CsV_3Sb_5 below its superconducting transition temperature, as shown in Fig. S11. If the observed hysteresis were due to trivial mechanisms, such as flux trapping, rather than intrinsic properties of the superconducting states, it should also appear in CsV_3Sb_5 as well. This result suggests that the superconducting states of RbV_3Sb_5 and CsV_3Sb_5 are different, and the hysteresis originates from the intrinsic superconducting properties of RbV_3Sb_5. It is interesting to note that Knight shift experiments in CsV_3Sb_5 suggested spin singlet pairing[44]. However, since our control experiments suggest that the superconducting properties of RbV_3Sb_5 are quite different from CsV_3Sb_5, the pairing symmetry of RbV_3Sb_5 is possibly unconventional.

Furthermore, the re-entrant superconductivity observed in our experiments is different from the re-entrance observed in conventional superconductors[45–47] which relies on vortex pinning induced by applied magnetic field. In contrast to some trivial re-entrant superconductivity observed only in specific directions, i.e. current parallel to magnetic field[46], in RbV_3Sb_5, the re-entrant superconductivity appears in all in-plane magnetic field directions with respect to a fixed current direction (as shown in Fig. S7 of Supplementary Information). What's more, the trivial reentrance induced by vortex pinning can only give rise to a symmetric B-T phase diagram[45,47]. This contradicts the asymmetric B-T phase diagram observed experimentally as shown in Fig. 3a.

Therefore, the simultaneous observation of both in-plane magnetic field hysteresis and asymmetric re-entrant superconductivity rules out trivial origins, indicating the need for a novel explanation.

Possible pairing symmetries

Considering the key observations in experiments reported above, we discuss the possible pairing symmetries in the kagome superconductor RbV_3Sb_5. First of all, the observed novel hysteresis in magnetoresistance measurements suggests spontaneous breaking of time-reversal symmetry, which is further corroborated by the zero-field superconducting diode effect observed in an irradiated RbV_3Sb_5 sample that breaks inversion symmetry (see Fig. S3 in the Supplementary Information for details). It is noted that the time-reversal symmetry may be broken in the normal states of the kagome family AV_3Sb_5 due to loop currents in the charge density wave phase[15,16,22,23]. However, the loop currents would produce out-of-plane magnetization, in contrast to the in-plane magnetic moments observed in this work. Therefore, the in-plane hysteresis is likely caused by the superconducting state itself, rather than the normal state. Moreover, as shown in Fig. 2g, the magnetoresistance hysteresis is weakened by the out-of-plane component of the magnetic field. The reason is as follows: RbV_3Sb_5 is a quasi-two-dimensional superconductor[48], where the out-of-plane resistivity is approximately 33 times greater than the in-plane resistivity at low temperatures. In such materials, an out-of-plane magnetic field rapidly suppresses superconductivity due to the orbital effects, which generates many vortices within the superconducting plane. When the applied magnetic field has a sizable out-of-plane component, many vortices will be created, and the vortices will dominate the transport properties of the superconducting films. As the transport is mostly dominated by vortices, the magnetoresistance behaves in a similar way for both the up-sweep and down-sweep fields, leading to the disappearance of hysteresis. A similar behavior is also observed in the heavy-fermion superconductor UCoGe[49], where a slight tilt of the magnetic field toward the c-axis leads to a significant decrease in the upper critical field and the disappearance of hysteresis.

In addition to the pronounced hysteresis, the observation of re-entrant superconductivity as the magnetic field increases suggests that the SC-II phase can be stabilized by the magnetic field. After carefully ruling out trivial origins, the spin-singlet scenario cannot support the field-induced re-entrant superconductivity. This is because the Zeeman effect of the magnetic field tends to suppress the spin-singlet superconducting state by inducing a depairing effect on spin-singlet Cooper pairs, whereas it does not affect the equal-spin pairing states. Therefore, the reappearance of the superconducting state under a larger magnetic field is not consistent with the spin-singlet Cooper pairs scenario. Instead, the observed re-entrance is more consistent with equal-spin pairing, where the spin-magnetic moments of the Cooper pairs couple to the magnetic field, lowering the energy of the superconducting state. Moreover, within the hysteresis loop, the transition of the finite resistance state to the superconducting state upon applying and then removing the current indicates that the finite resistance state is a metastable state. This suggests that there can be different superconducting domains with opposite spin polarizations in the finite resistance state, similar to the case of a ferromagnet with magnetic domains. Furthermore, due to the centrosymmetric point group symmetry, the superconducting pairing should be odd parity due to the spin-triplet pairing[50]. Therefore, the orbital part of the pairing should be p-wave or f-wave in nature[51–64]. These large number of novel properties observed in the superconducting state place strong constraints on the pairing symmetry of RbV_3Sb_5.

Since the superconducting pairing is formed near the Fermi surface, we project the four-orbital (eight-band) model into the manifestly covariant pseudospin basis (MCPB)[30,65,66] by choosing two degenerate bands ($|\mathbf{k},\alpha\rangle$, $|\mathbf{k},-\alpha\rangle$) near the Fermi surface as the projecting targets. Here, $\mathbf{k}$ is the crystal momentum and α is the pseudo-spin index (The detail can be found in the Method Section and the Supplementary Information). It is important to note that the original point group symmetry of the material is D_{6h}. Before the superconducting transition happens, the nematic order parameter comes in references[20,23] and reduces the point group symmetry to $\mathrm{D_{2h}}$. Therefore, the superconducting order parameters can be constructed by using basis functions belonging to irreducible representations of the point group $\mathrm{D_{2h}}$. As mentioned above, this pairing state must possess net in-plane spin polarization. The possible superconducting order parameters represented by the $\mathbf{d}$-vectors are listed in Table 1. Importantly, both of these are nodal topological p-wave, spin-triplet, time-reversal-symmetry-breaking states. As shown in the Supplementary Information, both of these states possess Majorana flat bands at the sample boundaries. In the following, we choose the $\mathrm{B_{3u}}$ representation without loss of generality.

The matrix representation of the superconducting gap in the MCPB is $\hat{\Delta}=(\mathbf{d}\cdot\boldsymbol{\sigma})i\sigma_2$, where the $\sigma_i (i=1,2,3)$ are the Pauli matrices. The nodes of these two order parameters belonging to different representations are located on x-axis and y-axis, respectively. The parameter $\boldsymbol{\xi}$ controls the amplitude of the spin polarization: $1-\eta=1-|\cos(2\boldsymbol{\xi})^2-\sin(2\boldsymbol{\xi})^2|$, which is determined by the specific form of the interactions in this material, while the parameter $\boldsymbol{\chi}$ controls the spin-polarization direction of the Cooper pairs. The orientation of the spin polarization $\mathbf{p}$ of the Cooper pair is given by: $\mathbf{p}=i\mathbf{d}\times\mathbf{d}^*\propto(\sin(\boldsymbol{\chi}),-\cos(\boldsymbol{\chi}),0)$, which is coupled with the effective magnetic field $\mathbf{g_k}$ in the MCPB in the form of $-\mathbf{g_k}\cdot\mathbf{p}$. Therefore, the direction of the spin polarization can be pinned by the applied magnetic field (See Supplementary Information for detail). When the magnetic field changes its sign, superconducting domains with opposite spin-polarization become energetically favorable and can be created.

A possible mechanism for the hysteresis, current heating and cooling experiments, and re-entrant superconductivity

Here, we provide a possible, schematic superconducting domain picture to explain the hysteresis in resistance, the current heating and cooling experiments as well as the reentrant superconductivity observed in $\mathrm{RbV_3Sb_5}$. As discussed in last section, the system has spin-polarized triplet pairing components which can form the superconducting domains[67,68] where Cooper pairs with net spin-polarization act like miniature magnets with different polarization directions, similar to ferromagnetic domains. At a low temperature for example (as denoted by $\mathrm{T_1}$ in Fig. 4), when the magnetic field sweeps from −1 T to 1 T, the system initially enters into a superconducting state dominated by negative domains. The negative domains are formed by spin-polarized Cooper pairs with magnetic moments pointing to the negative direction as indicated by blue arrows in Fig. 4. In other words, the spin-polarized Cooper pairs can form domains and the external magnetic field aligns the magnetization direction of the domains. When the magnetic field changes sign, superconducting domains with positive magnetization direction (positive domains) emerge. As the magnetic field further increases in the positive direction, positive domains become dominant, but the negative domains can still coexist. Therefore, at a positive magnetic field, we expect that the system enters into a metastable state characterized by the coexistence of the positive and negative domains as shown in Fig. 4. On the other hand, if the magnetic field is swept from 1 T to the same positive magnetic field, the domains are dominantly positive and the superconducting state will have a lower free energy. This provides a possible explanation for the hysteretic behavior of the resistance. Moreover, at a fixed positive magnetic field ~0.27 T (Fig. 2h), we can use a large current to heat the metastable finite-resistance state with both positive and negative domains and then remove the current under a fixed magnetic field, the system can transition to the superconducting ground state, where superconducting domains predominantly align with the applied

Table 1 | Possible order parameters with time-reversal symmetry breaking. Here $k_1=k_x$, $k_2=\frac{1}{2}k_x+\frac{\sqrt{3}}{2}k_y$

Representations	Order parameters
$\mathrm{B_{2u}}$	$\mathbf{d_{2u}}=(\sin(k_2-k_1)+\sin(k_2))(\cos(\boldsymbol{\chi})\cos(\boldsymbol{\xi}),\ \sin(\boldsymbol{\chi})\cos(\boldsymbol{\xi}), i\sin(\boldsymbol{\xi}))$
$\mathrm{B_{3u}}$	$\mathbf{d_{3u}}=\sin(k_1)(\cos(\boldsymbol{\chi})\cos(\boldsymbol{\xi}),\ \sin(\boldsymbol{\chi})\cos(\boldsymbol{\xi}), i\sin(\boldsymbol{\xi}))$

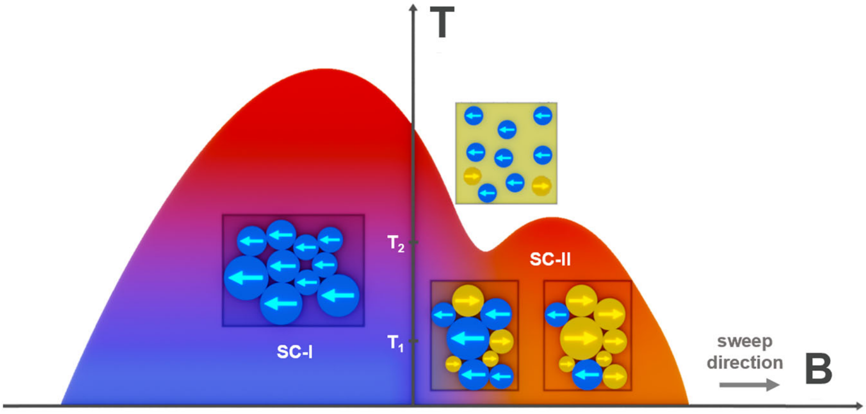

Fig. 4 | The schematics of the mechanism of spin-polarized p-wave superconductivity. Here 'T' and 'B' denote the temperature and the magnetic field, respectively. As the magnetic field sweeps from −1 T to 1 T, the system initially enters into a superconducting state dominated by 'negative' equal spin pairing domains, indicated by blue arrows in the first dome of superconductivity, namely SC-I. At a low-temperature $\mathrm{T_1}$, when the magnetic field changes sign, 'positive' domains, represented by yellow arrows, begin to proliferate. This coexistence of negative and positive superconducting domains results in the formation of a metastable state, SC-II, with higher free energy than SC-I. As a consequence, it reduces the transition temperature and the upper critical field, leading to an asymmetry between the two superconducting domes. At a high-temperature $\mathrm{T_2}$, when the magnetic field changes sign, the 'negative' domains become disconnected, and the system enters a finite-resistance state. At higher magnetic fields, the positive domains become more energetically favorable to form, and the proliferation and percolation of 'positive' domains lead to the second dome of superconductivity.

magnetic field. This current heating and cooling experiment strongly supports the superconducting domain picture of our theory which suggests that the SC-II state is a metastable state containing superconducting domains with different spin polarizations. In addition, in Fig. S13, three curves of distinct colors correspond to different initial magnetic fields (1 T for the black curve, 0 T for the blue curve, and −1 T for the red curve) at the onset of the field sweeping. These disparate trajectories, as illustrated in Fig. S13, indicate that the magnetic response of the superconducting state in RbV_3Sb_5 is determined by the initial magnetic field, thereby further supporting the domain picture.

At a higher temperature (as denoted by T_2 in Fig. 4), when the magnetic field sweeps from −1 T to 1 T, the system is initially in a superconducting state with negative domains. When the magnetic field changes sign from negative to positive, the negative domains shrink and the positive domains start to form as in the low temperature cases. However, due to the thermal effect, these domains are too small to be connected spatially to form a superconducting state. As the magnetic field increases, the positive domains become more energetically favorable to form. The enlargement of positive domains allows percolation of superconducting domains to give rise to superconducting state. This percolation picture gives a mechanism for the re-entrance of superconductivity at around 400 mK as observed in the experiment. Therefore, the nodal p-wave superconductivity belonging to the B_{2u} or the B_{3u} representation of the D_{2h} point group, which enables Cooper pairs exhibiting net spin-polarization, can provide a reasonable explanation of all the observed novel phenomena in RbV_3Sb_5.

In summary, we report experimental evidence for time-reversal-symmetry-breaking superconductivity in RbV_3Sb_5. This conclusion is supported by several experimental observations. First, we observed a magnetoresistance hysteresis in the superconducting state. Importantly, the superconducting diode effect in inversion-symmetry-broken samples at zero field clearly demonstrated the time-reversal symmetry breaking properties of the superconducting state. Furthermore, the magnetic hysteresis is absent in our CsV_3Sb_5 samples, which suggests distinct superconducting mechanisms in the two systems, despite both belonging to the same kagome family. Our work suggests RbV_3Sb_5 is a new platform for realizing unconventional and time-reversal symmetry breaking superconductivity.

Methods

Sample fabrication

The thin films of RbV_3Sb_5 were exfoliated using polydimethylsiloxane (PDMS) from the bulk crystal onto silicon substrates with a 285 nm oxide layer. The fabrication of pre-patterned metal electrodes was achieved using the standard electron-beam lithography (EBL) method, followed by deposition of a Ti/Au (10 nm/50 nm) through electron-beam evaporation. Then, the device was encapsulated with hBN to prevent any degradation due to air atmosphere. All device fabrication procedures mentioned above were performed in a controlled environment within a nitrogen-filled glovebox with oxygen and water levels below 0.01 ppm to minimize any potential degradation of the samples.

Quantum transport measurements

The samples were measured in an Oxford dilution refrigerator Triton XL1000 equipped with a vector magnet. This setup allowed the samples to remain stationary while a real three-dimensional vector magnetic field was applied. Such a technique greatly improves the precision of the magnetic field angle-deviation measurements, effectively circumventing the issues of return differences and heat generation commonly associated with mechanical rotators.

The dV/dI measurements were conducted with a rather small alternative current (i.e., 100 nA or 10 nA) while applying a much larger direct current (i.e., 10 μA). To optimize the signal-to-noise ratio in these experiments, a standard lock-in technique was employed, along with the implementation of essential low-temperature filters.

Conducting the strict in-plane magnetic field measurements with the 3D vector magnet

1. Initially, we securely mounted the sample within the dilution refrigerator. Despite our meticulous efforts to align the sample with the magnetic field axis, a minor discrepancy persisted.
2. In response to this, our subsequent step involved the calibration of the vector magnetic field. What sets our approach apart from the traditional mechanical rotational system is that we did not need to physically rotate the sample plane, we could fine-tune the value of the vector magnetic field, which would greatly enhance the angle accuracy.
3. During the calibration process, we initially conducted angle-dependent measurements of the critical magnetic field of the sample in both the XZ and YZ planes. Given that our sample plane was mounted in the XY plane, these measurements allowed us to determine the angle deviation from the sample plane. With the calibration of the XZ-plane and YZ-plane, then the new coordinates are achieved, with strict alignment of the vector magnetic field within the XY plane. It's worth noting that our device substrate consisted of a rigid silicon wafer with a 285 nm SiO_2 layer. Through this dual-axis calibration process, we can confidently assert that the calibrated XY plane remains strictly within the sample plane, with an error margin of less than 0.1°.

Ruling out trivial origins of two-fold symmetric superconductivity

It has been suggested that the anisotropy may arise from current-induced vortex motion. Such a scenario was ruled out by different configurations in our previous paper[69]. The two-fold symmetric axis is independent on the current direction. Specifically speaking, in both cases that the current is applied in-plane with $\phi = 90°$ and $\phi = 0°$, the in-plane azimuthal angular dependence of the magnetoresistance exhibited the same twofold symmetry pattern, irrespective of the current direction. Thus, the two-fold symmetry is independent of the current direction, ruling out the possible vortex origin.

Manifestly covariant pseudospin basis (MCPB)

Due to the existence of the inversion symmetry, though there is SOPC[30,31], one can always define a pseudospin basis, in which the orbital and pseudospin degrees of freedom are decoupled. On the other hand, since the superconducting pairing happens near the Fermi surface, we can project the four-orbital (eight-band) model into a two degenerate band basis with different pseudospins, which is named as the manifestly covariant pseudospin basis (MCPB)[30,65,66]. In this basis, the magnetic field couples to the spin in this form:

$$H_Z = \mu_B \sum_{\mathbf{k},\alpha,\beta,i,j} c^{\dagger}_{\mathbf{k}\alpha} B_i a_{ij}(\mathbf{k}) \sigma_j^{\alpha\beta} c_{\mathbf{k}\beta}, \tag{1}$$

where μ_B means the Bohr magnetron, α, β label the pseudospin of the fermion in band basis, $\sigma_i (i = 1,2,3)$ are Pauli metrices. Here, $a_{ij}(\mathbf{k}) (i,j = 1,2,3)$ come from the projection to MCPB (See Supplementary Information for detail), which change the original magnetic field B_i into a $\mathbf{k}$-dependent effective magnetic field $\mathbf{g_k} = \mu_B \bar{a}_{\mathbf{k}} \boldsymbol{B}$. Including the pairing order parameter, the total Hamiltonian of the superconducting state can be written as:

$$H_{total} = \sum_{\mathbf{k},\alpha} \varepsilon_{\mathbf{k}} c^{\dagger}_{\mathbf{k}\alpha} c_{\mathbf{k}\alpha} + \sum_{\mathbf{k}\alpha\beta} \left(c^{\dagger}_{\mathbf{k}\alpha} [(\mathbf{d} \cdot \boldsymbol{\sigma}) i\sigma_2]_{\alpha\beta} c^{\dagger}_{-\mathbf{k}\beta} + h.c. \right) + H_z, \tag{2}$$

where the $\mathbf{d}$-vector is the possible order parameter of the odd-parity superconductivity which is show in Table 1. With the total Hamiltonian

H_{total}, one can calculate the topological properties and the magnetic responses conveniently. Importantly, this Hamiltonian describes a nodal topological p-wave superconductor which possesses the Majorana flat bands[70–77] on the edges of the samples[78–82] (See Fig. S13 in Supplementary Information for the result of the open boundary calculations).

Data availability

The data that support the plots within this paper and other related findings are available from the corresponding author upon request. Alternatively, the data can be accessed through the database at the following link https://doi.org/10.6084/m9.figshare.30354730.

References

1. Ortiz, B. R. et al. New kagome prototype materials: discovery of KV_3Sb_5, RbV_3Sb_5, and CsV_3Sb_5. *Phys. Rev. Mater.* **3**, 094407 (2019).
2. Yin, J.-X., Lian, B. & Hasan, M. Z. Topological kagome magnets and superconductors. *Nature* **612**, 647–657 (2022).
3. Jiang, K. et al. Kagome superconductors AV_3Sb_5(A = K, Rb, Cs). *Natl. Sci. Rev.* **10**, nwac199 (2023).
4. Wang, Y., Wu, H., McCandless, G. T., Chan, J. Y. & Ali, M. N. Quantum states and intertwining phases in kagome materials. *Nat. Rev. Phys.* **5**, 635–658 (2023).
5. Zheng, L. et al. Emergent charge order in pressurized kagome superconductor CsV_3Sb_5. *Nature* **611**, 682–687 (2022).
6. Chen, H. et al. Roton pair density wave in a strong-coupling kagome superconductor. *Nature* **599**, 222–228 (2021).
7. Liang, Z. et al. Three-Dimensional Charge Density Wave and Surface-Dependent Vortex-Core States in a Kagome Superconductor CsV_3Sb_5. *Phys. Rev. X* **11**, 031026 (2021).
8. Wu, X. et al. Nature of Unconventional Pairing in the Kagome Superconductors AV_3Sb_5(A = K, Rb, Cs). *Phys. Rev. Lett.* **127**, 177001 (2021).
9. Guguchia, Z. et al. Tunable unconventional kagome superconductivity in charge ordered RbV_3Sb_5 and KV_3Sb_5. *Nat. Commun.* **14**, 153 (2023).
10. Yu, F. H. et al. Unusual competition of superconductivity and charge-density-wave state in a compressed topological kagome metal. *Nat. Commun.* **12**, 3645 (2021).
11. Zhao, H. et al. Cascade of correlated electron states in the kagome superconductor CsV_3Sb_5. *Nature* **599**, 216–221 (2021).
12. Deng, H. et al. Chiral kagome superconductivity modulations with residual Fermi arcs. *Nature* **632**, 775–781 (2024).
13. Yan, X.-Y. et al. Chiral Pair Density Waves with Residual Fermi Arcs in RbV_3Sb_5. *Chin. Phys. Lett.* **41**, 097401 (2024).
14. Le, T. et al. Superconducting diode effect and interference patterns in kagome CsV_3Sb_5. *Nature* **630**, 64–69 (2024).
15. van Heumen, E. Kagome lattices with chiral charge density. *Nat. Mater.* **20**, 1304–1314 (2021).
16. Jiang, Y.-X. et al. Unconventional chiral charge order in kagome superconductor KV_3Sb_5. *Nat. Mater.* **20**, 1353–1357 (2021).
17. Li, H. et al. Rotation symmetry breaking in the normal state of a kagome superconductor KV_3Sb_5. *Nat. Phys.* **18**, 265–270 (2022).
18. Fernandes, R. M. Kagome superconductors charge ahead. *Nat. Mater.* **22**, 151–152 (2022).
19. Kang, M. et al. Charge order landscape and competition with superconductivity in kagome metals. *Nat. Mater.* **22**, 186–193 (2022).
20. Nie, L. et al. Charge-density-wave-driven electronic nematicity in a kagome superconductor. *Nature* **604**, 59–64 (2022).
21. Saykin, D. R. et al. High Resolution Polar Kerr Effect Studies of CsV_3Sb_5: Tests for Time-Reversal Symmetry Breaking below the Charge-Order Transition. *Phys. Rev. Lett.* **131**, 016901 (2023).
22. Feng, X., Jiang, K., Wang, Z. & Hu, J. Chiral flux phase in the Kagome superconductor AV_3Sb_5. *Sci. Bull.* **66**, 1384–1388 (2021).
23. Xu, Y. et al. Three-state nematicity and magneto-optical Kerr effect in the charge density waves in kagome superconductors. *Nat. Phys.* **18**, 1470–1475 (2022).
24. Feng, X., Zhang, Y., Jiang, K. & Hu, J. Low-energy effective theory and symmetry classification of flux phases on the kagome lattice. *Phys. Rev. B* **104**, 165136 (2021).
25. Xing, Y. et al. Optical manipulation of the charge-density-wave state in RbV_3Sb_5. *Nature* **631**, 60–66 (2024).
26. Xu, H.-S. et al. Multiband Superconductivity with Sign-Preserving Order Parameter in Kagome Superconductor CsV_3Sb_5. *Phys. Rev. Lett.* **127**, 187004 (2021).
27. Roppongi, M. et al. Bulk evidence of anisotropic s-wave pairing with no sign change in the kagome superconductor CsV_3Sb_5. *Nat. Commun.* **14**, 667 (2023).
28. Zhong, Y. et al. Nodeless electron pairing in CsV_3Sb_5-derived kagome superconductors. *Nature* **617**, 488–492 (2023).
29. Gu, Y., Zhang, Y., Feng, X., Jiang, K. & Hu, J. Gapless excitations inside the fully gapped kagome superconductors AV_3Sb_5. *Phys. Rev. B* **105**, L100502 (2022).
30. Xie, Y.-M., Zhou, B. T. & Law, K. T. Spin-Orbit-Parity-Coupled Superconductivity in Topological Monolayer WTe_2. *Phys. Rev. Lett.* **125**, 107001 (2020).
31. Zhang, E. et al. Spin–orbit–parity coupled superconductivity in atomically thin 2M-WS_2. *Nat. Phys.* **19**, 106–113 (2022).
32. Michael Tinkham. *Introduction to Superconductivity*.
33. Caswell, H. L. Magnetic Hysteresis in Superconducting Thin Films. *J. Appl. Phys.* **36**, 80–84 (1965).
34. Dew-Hughes, D. The critical current of superconductors: an historical review. *Low. Temp. Phys.* **27**, 713–722 (2001).
35. W. Lawrence & S. Doniach. *Proceedings of the 12th International Conference on Low Temperature Physics: Kyoto, Japan, September* 4–10, 1970. (Academic Press of Japan, 1971).
36. Yuan, N. F. Q. Orbital Fulde-Ferrell-Larkin-Ovchinnikov state in an Ising superconductor. *Phys. Rev. Res.* **5**, 043122 (2023).
37. Cao, Y., Park, J. M., Watanabe, K., Taniguchi, T. & Jarillo-Herrero, P. Pauli-limit violation and re-entrant superconductivity in moiré graphene. *Nature* **595**, 526–531 (2021).
38. Ji, L., Rzchowski, M. S., Anand, N. & Tinkham, M. Magnetic-field-dependent surface resistance and two-level critical-state model for granular superconductors. *Phys. Rev. B* **47**, 470–483 (1993).
39. Semenov, S. V. & Balaev, D. A. Magnetoresistance Hysteresis Evolution in the Granular Y–Ba–Cu–O High-Temperature Superconductor in a Wide Temperature Range. *J. Supercond. Nov. Magn.* **32**, 2409–2419 (2019).
40. Semenov, S. V., Balaev, D. A. & Petrov, M. I. Universal Behavior and Temperature Evolution of the Magnetoresistance Hysteresis in Granular High-Temperature Superconductors Y–Ba–Cu–O. *Phys. Solid State* **63**, 1069–1080 (2021).
41. Ginzburg, V. L. On the destruction and the onset of superconductivity in a magnetic field. *Sov. Phys. JETP* **34**, 1 (1958).
42. Muné, P., Fonseca, F. C., Muccillo, R. & Jardim, R. F. Magnetic hysteresis of the magnetoresistance and the critical current density in polycrystalline YBa2Cu3O7−δ–Ag superconductors. *Phys. C: Superconductivity* **390**, 363–373 (2003).
43. García-Fornaris, I., Govea-Alcaide, E., Muné, P. & Jardim, R. F. Magnetoresistance, transport noise and granular structure in polycrystalline superconductors. *Phys. Status Solidi (a)* **204**, 805–813 (2007).
44. Mu, C. et al. S-Wave Superconductivity in Kagome Metal CsV_3Sb_5 Revealed by$^{121/123}$ Sb NQR and^{51} V NMR Measurements. *Chin. Phys. Lett.* **38**, 077402 (2021).
45. Córdoba, R. et al. Magnetic field-induced dissipation-free state in superconducting nanostructures. *Nat. Commun.* **4**, 1437 (2013).

46. Wang, Y.-L. et al. Parallel magnetic field suppresses dissipation in superconducting nanostrips. *Proc. Natl. Acad. Sci.* **114**, E10274–E10280 (2017).
47. Zhang, E. et al. Magnetic-Field-Induced Re-entrance of Superconductivity in Ta_2PdS_5 Nanostrips. *Nano Lett.* **21**, 288–297 (2021).
48. Yin, Q. et al. Superconductivity and Normal-State Properties of Kagome Metal RbV_3Sb_5 Single Crystals. *Chin. Phys. Lett.* **38**, 037403 (2021).
49. Steven, E. et al. Robust properties of the superconducting ferromagnet UCoGe. *Appl. Phys. Lett.* **98**, 132507 (2011).
50. Ghosh, S. K. et al. Recent progress on superconductors with time-reversal symmetry breaking. *J. Phys.: Condens. Matter* **33**, 033001 (2021).
51. Leggett, A. J. A theoretical description of the new phases of liquid ^{3}He. *Rev. Mod. Phys.* **47**, 331–414 (1975).
52. Sigrist, M. & Ueda, K. Phenomenological theory of unconventional superconductivity. *Rev. Mod. Phys.* **63**, 239–311 (1991).
53. Lee, D. M. The extraordinary phases of liquid ^{3}He. *Rev. Mod. Phys.* **69**, 645-666 (1997).
54. Strand, J. D., Van Harlingen, D. J., Kycia, J. B. & Halperin, W. P. Evidence for Complex Superconducting Order Parameter Symmetry in the Low-Temperature Phase of UPt_3 from Josephson Interferometry. *Phys. Rev. Lett.* **103**, 197002 (2009).
55. Kidwingira, F., Strand, J. D., Van Harlingen, D. J. & Maeno, Y. Dynamical Superconducting Order Parameter Domains in Sr_2RuO_4. *Science* **314**, 1267–1271 (2006).
56. Mackenzie, A. P. & Maeno, Y. The superconductivity of Sr_2RuO_4 and the physics of spin-triplet pairing. *Rev. Mod. Phys.* **75**, 657 (2003).
57. Strand, J. D. et al. The Transition Between Real and Complex Superconducting Order Parameter Phases in UPt_3. *Science* **328**, 1368–1369 (2010).
58. Schemm, E. R., Gannon, W. J., Wishne, C. M., Halperin, W. P. & Kapitulnik, A. Observation of broken time-reversal symmetry in the heavy-fermion superconductor UPt_3. *Science* **345**, 190–193 (2014).
59. Ran, S. et al. Nearly ferromagnetic spin-triplet superconductivity. *Science* **365**, 684–687 (2019).
60. Jiao, L. et al. Chiral superconductivity in heavy-fermion metal UTe_2. *Nature* **579**, 523–527 (2020).
61. Hayes, I. M. et al. Multicomponent superconducting order parameter in UTe_2. *Science* **373**, 797–801 (2021).
62. Gu, Q. et al. Detection of a pair density wave state in UTe_2. *Nature* **618**, 921–927 (2023).
63. Pustogow, A. et al. Constraints on the superconducting order parameter in Sr_2RuO_4 from oxygen–17 nuclear magnetic resonance. *Nature* **574**, 72–75 (2019).
64. Kinjo, K. et al. Superconducting spin smecticity evidencing the Fulde-Ferrell-Larkin-Ovchinnikov state in Sr_2RuO_4. *Science* **376**, 397–400 (2022).
65. Fu, L. Parity-Breaking Phases of Spin-Orbit-Coupled Metals with Gyrotropic, Ferroelectric, and Multipolar Orders. *Phys. Rev. Lett.* **115**, 026401 (2015).
66. Fischer, M. H., Sigrist, M., Agterberg, D. F. & Yanase, Y. Superconductivity and Local Inversion-Symmetry Breaking. *Annu. Rev. Condens. Matter Phys.* **14**, 153–172 (2023).
67. Xia, J., Maeno, Y., Beyersdorf, P. T., Fejer, M. M. & Kapitulnik, A. High Resolution Polar Kerr Effect Measurements of Sr_2RuO_4: Evidence for Broken Time-Reversal Symmetry in the Superconducting State. *Phys. Rev. Lett.* **97**, 167002 (2006).
68. Day, C. Superconductor forms domains that break time-reversal symmetry. *Phys. Today* **59**, 23–27 (2006).
69. Wang, S. et al. Two-fold symmetric superconductivity in the Kagome superconductor RbV_3Sb_5. *Commun. Phys.* **7**, 15 (2024).
70. Sato, M. & Fujimoto, S. Topological phases of noncentrosymmetric superconductors: Edge states, Majorana fermions, and non-Abelian statistics. *Phys. Rev. B* **79**, 094504 (2009).
71. Hasan, M. Z. & Kane, C. L. *Colloquium*: Topological insulators. *Rev. Mod. Phys.* **82**, 3045–3067 (2010).
72. Sato, M. & Fujimoto, S. Existence of Majorana Fermions and Topological Order in Nodal Superconductors with Spin-Orbit Interactions in External Magnetic Fields. *Phys. Rev. Lett.* **105**, 217001 (2010).
73. Schnyder, A. P. & Ryu, S. Topological phases and surface flat bands in superconductors without inversion symmetry. *Phys. Rev. B* **84**, 060504 (2011).
74. Qi, X.-L. & Zhang, S.-C. Topological insulators and superconductors. *Rev. Mod. Phys.* **83**, 1057–1110 (2011).
75. Alicea, J. New directions in the pursuit of Majorana fermions in solid state systems. *Rep. Prog. Phys.* **75**, 076501 (2012).
76. Beenakker, C. W. J. Search for Majorana Fermions in Superconductors. *Annu. Rev. Condens. Matter Phys.* **4**, 113–136 (2013).
77. Wong, C. L. M., Liu, J., Law, K. T. & Lee, P. A. Majorana flat bands and unidirectional Majorana edge states in gapless topological superconductors. *Phys. Rev. B* **88**, 060504 (2013).
78. Fu, L. & Kane, C. L. Superconducting Proximity Effect and Majorana Fermions at the Surface of a Topological Insulator. *Phys. Rev. Lett.* **100**, 096407 (2008).
79. Tewari, S., Das Sarma, S., Nayak, C., Zhang, C. & Zoller, P. Quantum Computation using Vortices and Majorana Zero Modes of a $p_x + ip_y$ Superfluid of Fermionic Cold Atoms. *Phys. Rev. Lett.* **98**, 010506 (2007).
80. Elliott, S. R. & Franz, M. *Colloquium*: Majorana fermions in nuclear, particle, and solid-state physics. *Rev. Mod. Phys.* **87**, 137–163 (2015).
81. Lutchyn, R. M. et al. Majorana zero modes in superconductor–semiconductor heterostructures. *Nat. Rev. Mater.* **3**, 52–68 (2018).
82. Prada, E. et al. From Andreev to Majorana bound states in hybrid superconductor–semiconductor nanowires. *Nat. Rev. Phys.* **2**, 575 (2020).

Acknowledgements

This work was supported by the National Key Research and Development Program of China (Grants No. 2020YFA0309300, 2022YFA1403700), the National Natural Science Foundation of China (Grants No. 12074162, 12004158, 91964201), Guangdong Basic and Applied Basic Research Foundation (Grant No. 2022B1515130005), Quantum Science and Technology-National Science and Technology Major Project (Grants No. 2021ZD0303000 and 2021ZD0303001). K.T. L. acknowledges the support of the Ministry of Science and Technology, China, and Hong Kong Research Grant Council through Grants No. 2020YFA0309600, RFS2021-6S03, C6025–19G, C6053-23G, AoE/P-701/20, 16310520, 16310219, 16307622, 16311424 and 16309223.

Author contributions

B.-C.L. supervised the project and conceived and designed the experiments. S. W. and B.-C.L. did the quantum transport experiments with J.-J.Z.'s software support. S.W. and J.-Z.F. fabricated and characterized samples with necessary assistance of J.-P.P., J.-J.Y., D.Y. and Z.Z. J.-J.Y. and J.-P.P. did the AFM experiments. J.L. and Xuewen F. did the HRTEM experiments. N.K. and X.-S.W. helped with the understanding of experiments. Xilin F., Z.-T.S., and K.T.L. proposed the theory. B.-C.L., Xilin F., and K.T.L. wrote the manuscript with inputs from all authors.

Competing interests

The authors declare no competing interests.

Additional information

Supplementary information The online version contains supplementary material available at https://doi.org/10.1038/s41467-025-68067-8.

Correspondence and requests for materials should be addressed to Kam Tuen Law, Ben-Chuan Lin or Dapeng Yu.

Peer review information *Nature Communications* thanks Sylvia Lewin, and the other, anonymous, reviewer(s) for their contribution to the peer review of this work. A peer review file is available.

Reprints and permissions information is available at http://www.nature.com/reprints

Publisher's note Springer Nature remains neutral with regard to jurisdictional claims in published maps and institutional affiliations.

Open Access This article is licensed under a Creative Commons Attribution-NonCommercial-NoDerivatives 4.0 International License, which permits any non-commercial use, sharing, distribution and reproduction in any medium or format, as long as you give appropriate credit to the original author(s) and the source, provide a link to the Creative Commons licence, and indicate if you modified the licensed material. You do not have permission under this licence to share adapted material derived from this article or parts of it. The images or other third party material in this article are included in the article's Creative Commons licence, unless indicated otherwise in a credit line to the material. If material is not included in the article's Creative Commons licence and your intended use is not permitted by statutory regulation or exceeds the permitted use, you will need to obtain permission directly from the copyright holder. To view a copy of this licence, visit http://creativecommons.org/licenses/by-nc-nd/4.0/.

© The Author(s) 2026